

# Observations of the low-luminosity Type Iax supernova 2019gsc: a fainter clone of SN 2008ha?\*

Lina Tomasella,<sup>1,†</sup> Maximilian Stritzinger,<sup>2</sup> Stefano Benetti,<sup>1</sup> Nancy Elias-Rosa,<sup>1,3</sup> Enrico Cappellaro,<sup>1</sup> Erkki Kankare,<sup>4</sup> Peter Lundqvist,<sup>5,6</sup> Mark Magee,<sup>7</sup> Kate Maguire,<sup>7</sup> Andrea Pastorello,<sup>1</sup> Simon Prentice,<sup>7</sup> Andrea Reguitti<sup>1,8,9</sup>

<sup>1</sup>INAF Osservatorio Astronomico di Padova, Vicolo dell'Osservatorio 5, 35122 Padova, Italy

<sup>2</sup>Department of Physics and Astronomy, Aarhus University, Ny Munkegade 120, DK-8000 Aarhus C, Denmark

<sup>3</sup>Institute of Space Sciences (ICE, CSIC), Campus UAB, Carrer de Can Magrans s/n, 08193 Barcelona, Spain

<sup>4</sup>Tuorla Observatory, Department of Physics and Astronomy, University of Turku, FI-20014 Turku, Finland

<sup>5</sup>Department of Astronomy, AlbaNova University Center, Stockholm University, SE-10691 Stockholm, Sweden

<sup>6</sup>The Oskar Klein Centre, AlbaNova, SE-10691 Stockholm, Sweden

<sup>7</sup>School of Physics, Trinity College Dublin, Dublin 2, Ireland

<sup>8</sup>Millennium Institute of Astrophysics (MAS), Nuncio Monseñor Sotero Sanz 100, Providencia, Santiago, Chile

<sup>9</sup>Departamento de Ciencias Físicas, Universidad Andres Bello, Fernandez Concha 700, Las Condes, Santiago, Chile

Accepted MNRAS

## ABSTRACT

We present optical photometric and spectroscopic observations of the faint-and-fast evolving type Iax SN 2019gsc, extending from the time of  $g$ -band maximum until about fifty days post maximum, when the object faded to an apparent  $r$ -band magnitude  $m_r = 22.48 \pm 0.11$  mag. SN 2019gsc reached a peak luminosity of only  $M_g = -13.58 \pm 0.15$  mag, and is characterised with a post-maximum decline rate  $\Delta m_{15}(g) = 1.08 \pm 0.14$  mag. These light curve parameters are comparable to those measured for SN 2008ha of  $M_g = -13.89 \pm 0.14$  mag at peak and  $\Delta m_{15}(g) = 1.80 \pm 0.03$  mag. The spectral features of SN 2019gsc also resemble those of SN 2008ha at similar phases. This includes both the extremely low ejecta velocity at maximum,  $\sim 3,000$  km s<sup>-1</sup>, and at late-time (phase +54 d) strong forbidden iron and cobalt lines as well as both forbidden and permitted calcium features. Furthermore, akin to SN 2008ha, the bolometric light curve of SN 2019gsc is consistent with the production of  $\approx 0.003 \pm 0.001$  M<sub>⊙</sub> of <sup>56</sup>Ni. The explosion parameters,  $M_{ej} \approx 0.13$  M<sub>⊙</sub> and  $E_k \approx 12 \times 10^{48}$  erg, are also similar to those inferred for SN 2008ha. We estimate a sub-solar oxygen abundance for the host galaxy of SN 2019gsc ( $12 + \log_{10}(\text{O}/\text{H}) = 8.10 \pm 0.18$  dex), consistent with the equally metal-poor environment of SN 2008ha. Altogether, our dataset for SN 2019gsc indicates that this is a member of a small but growing group of extreme SN Iax that includes SN 2008ha and SN 2010ae.

**Key words:** supernovae: general – supernovae: individual: SN 2019gsc (AT-LAS19mbg, PS19bex, ZTF19aawhlc)

## 1 INTRODUCTION

Type Iax supernovae (hereafter SNe Iax), also known as 2002cx-like SNe after their prototype described by Li et al. (2003), are possibly a class of thermonuclear explosions showing some spectroscopic similarities to SNe Ia near maximum light, while at late-time they appear significantly different (e.g., Foley et al. 2016; Jha 2017). In fact, at early epochs SNe Iax exhibit features of Fe III and therefore resemble over-luminous 1991T-like SNe at similar phases. However, their late spectra are dominated by prevalent Ca II per-

\* This paper includes data gathered with the 2.56-m Nordic Optical Telescope, the 10.4-m Gran Telescopio Canarias and the Liverpool Telescope located at the Observatorio del Roque de los Muchachos, La Palma, Spain. It also includes data obtained with Las Cumbres Observatory global network. Data available on request.

† E-mail: lina.tomasella@inaf.it

mitted and forbidden spectral lines in complete contrast to SNe Ia that are instead dominated by broad, forbidden [Fe II] and [Fe III] emission features. Interestingly, the energetics of SNe Iax explosions and their luminosities can be very different from one event to the other: within the class, peak absolute magnitudes range from  $M_{peak} \approx -13$  mag for the fainter members to  $M_{peak} \approx -19$  mag for the brighter ones (the latter close to the peak luminosity of normal SNe Ia; cf. Jha 2017, see his Table 1). In all cases, SNe Iax show maximum-light expansion velocities measured from the Si II  $\lambda 6355$  line that are much lower than those measured in SNe Ia. Quantitatively, at maximum the expansion velocities in SNe Ia are typically around  $\sim 10,000$  km s<sup>-1</sup>, while the velocities inferred from SNe Iax never exceed 7,000 km s<sup>-1</sup>, and can be as low as 2,000 km s<sup>-1</sup>.

The above mentioned peculiar traits of SNe Iax, particularly of the fainter members of the class such as SN 2008ha and SN 2010ae (Foley et al. 2009; Valenti et al. 2009; Stritzinger et al. 2014), have brought out a variety of models and explosion scenarios (see the review by Jha 2017), including a core-collapse, massive star supernova origin (Moriya et al. 2010). However, the bunch of the observational characteristics of SNe Iax suggests their close affinity to normal type Ia SNe and to several other classes of peculiar SNe Ia (cf. Taubenberger 2017). Thus, the thermonuclear explosion of a carbon-oxygen Chandrasekhar-mass ( $M_{Ch}$ ) white dwarf (WD) in a binary system is the leading scenario that has emerged gradually over time (Foley et al. 2009; Stritzinger et al. 2014, 2015; Jha 2017).

In the context of the thermonuclear explosion of WDs, a number of alternatives have been proposed to account for the origins of SNe Iax and to explain the diversity in luminosities and explosion energies among the members of the class, from *failed* deflagrations that leave a bound remnant (which is a natural outcome of 3D models with off-centre ignition, cf. Nonaka, et al. 2012) to pulsational delayed detonations (i.e. for the brightest SNe 2005hk or 2012Z, see Stritzinger et al. 2015). The direct detection of a blue source at the location of SN 2012Z in pre-explosion *Hubble Space Telescope* (HST) images by McCully et al. (2014) suggested a helium-star donating material to an accreting WD as the progenitor of this event, similarly to the Galactic helium nova V445-Pup (McCully et al. 2014).

Pure deflagration models of carbon-oxygen (C/O) WDs or hybrid carbon-oxygen-neon (C/O/Ne) WDs in binary systems (likely with a He-star companion), as developed by Jordan et al. (2012); Kromer et al. (2013); Fink et al. (2014); Kromer et al. (2015), can replicate the overall properties of intermediate-to-bright SNe Iax. However, some difficulties have arisen with the faintest members of the class, i.e. in reproducing the observed amount of nickel (it is too large in Fink et al. 2014 models), or ejecta mass (it is too small in Kromer et al. 2015 simulations). Thus, in order to test the various models proposed for SNe Iax, including the merger of C/O–O/Ne WDs as in the double-degenerate scenario of Kashyap et al. (2018), a larger observational dataset of SNe Iax is needed, especially of the low end of the peak luminosity distribution.

Soon after discovery, Leloudas et al. (2019) provided the spectroscopic classification of SN 2019gsc as a type Iax event. Furthermore, the peculiar nature of this object was noted, as it closely resembled the type Iax SNe 2008ha and

2010ae (Foley et al. 2009; Valenti et al. 2009; Stritzinger et al. 2014), the faintest and least-energetic SNe Iax yet observed. The preliminary photometric observations of SN 2019gsc indicated that it could be even fainter than the extreme SN 2008ha. This paper presents optical spectroscopic and photometric observations of SN 2019gsc that, as we will show, shares many characteristics with both SN 2008ha and SN 2010ae over its entire evolution. The manuscript is organized as follows: in Section 2 we provide basic information about the SN discovery, its host galaxy, our observations and the data reduction procedures. In Section 3, the photometric evolution and photometric parameters of SN 2019gsc are presented, while the spectroscopic analysis is reported in Section 4. In Section 5 we examine the environment of SN 2019gsc and set it in context with that of other faint SNe Iax. Discussion and conclusions are in Section 6. Another paper on SN 2019gsc by Srivastav, et al. (2020) was submitted for publication almost simultaneously to this work. A brief comparison of the results of these independent investigations is also reported in the final section.

## 2 DISCOVERY AND FOLLOW-UP OBSERVATIONS OF SN 2019GSC

SN 2019gsc (also known as ATLAS19mbg, PS19bex and ZTF19aawhlc) was discovered on 2019 June 02.35 UT by the ATLAS (Asteroid Terrestrial-impact Last Alert System) Project (Tonry, et al. 2018), at a cyan-ATLAS AB magnitude of 19.66 (Smartt, et al. 2019, see also Tonry et al. 2019, TNS Astronomical Transient Report No. 36575). The discovery report also noted a non-detection two days earlier (2019 May 31.39 UT) although in a different filter (orange-ATLAS) and not very deep (19.34 mag). The SN is located in the irregular galaxy SBS 1436+529A (other name: PGC052275), see Fig. 1, which is characterized by the presence of clumpy H II regions, similarly to SN 2008ha’s host-galaxy UGG 12682. The galaxy is described as a merging system, with two nuclei separated by 3.8 arcsec, which corresponds to 0.9 kpc (Huchtmeier et al. 2008).

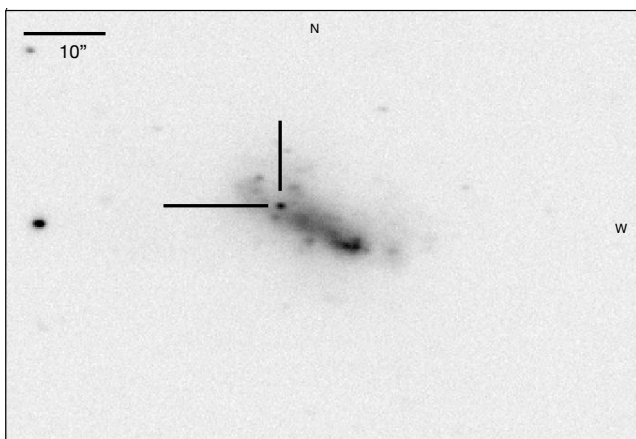
A heliocentric recessional velocity of  $3384 \pm 3$  km s<sup>-1</sup> for SBS 1436+529A is reported in the NASA/IPAC Extragalactic Database (NED) estimated from the Sloan Digital Sky Survey Data Release 3<sup>1</sup> observations. Adopting  $H_0 = 73.2 \pm 1.7$  km s<sup>-1</sup> Mpc<sup>-1</sup> (Riess et al. 2016) and corrections for peculiar motions due to influences of the Virgo cluster, the Great Attractor, and the Shapley supercluster (Mould et al. 2000), we obtain a Hubble flow distance and distance modulus to the host of SN 2019gsc of  $53.4 \pm 3.7$  Mpc and  $\mu = 33.64 \pm 0.15$  mag, respectively. The NED database also provides a Milky Way reddening in the direction of SBS 1436+529A of  $E(B-V)_{MW} = 0.008 \pm 0.005$  mag (Schlafly & Finkbeiner 2011). We do not detect interstellar Na I D lines at the redshift of the host, therefore we assume that the reddening in the host of SN 2019gsc is minimal.

A spectrum of SN 2019gsc was obtained a day after discovery, on 2019 June 03.97 UT (Leloudas et al. 2019) with the Nordic Optical Telescope 2.56m (NOT), and it was

<sup>1</sup> <http://www.sdss.org/dr3/products/spectra/getspectra.html>

**Table 1.** Basic information on SN 2019gsc and its host-galaxy.

Host galaxy	SBS 1436+529A (PGC052275)
Galaxy type	Irregular
Heliocentric radial velocity	$3384 \pm 3 \text{ km s}^{-1}$
Redshift ( $z$ )	0.011288
Distance modulus	$33.64 \pm 0.15 \text{ mag}$
Galactic extinction	$E(B - V)_{MW} = 0.008 \pm 0.005 \text{ mag}$ ( $A_B = 0.034 \text{ mag}$ , $A_V = 0.026 \text{ mag}$ )
SN spectral type	Iax
RA (J2000.0)	$14^{\text{h}}37^{\text{m}}45.24^{\text{s}}$
Dec (J2000.0)	$+52^{\circ}43'36.43''$
Discovery date	2019-06-02 08:31:12 UT (ATLAS cyan mag 19.66)
Last no-detection	2019-05-31 09:27:21 UT
Date of $g$ -band maximum	2019-06-01 (MJD 58635.4)
Date of $r$ -band maximum	2019-06-07 (MJD 58641.4)
$m_g$ at maximum	$19.92 \pm 0.01 \text{ mag}$
$M_g$ at maximum	$-13.58 \pm 0.15 \text{ mag}$
$m_r$ at maximum	$19.46 \pm 0.01 \text{ mag}$
$M_r$ at maximum	$-14.28 \pm 0.15 \text{ mag}$
$\Delta m_{15}(g)$	$1.08 \pm 0.06 \text{ mag}$
$L_{\text{bol}}$ at maximum	$\approx 10^{41} \text{ erg s}^{-1}$

**Figure 1.** Finding chart of SBS 1436+529A (PGC052275) constructed with a  $g$ -band image obtained with the NOT (+ AL-FOSC) on 2019 June 07. The position of SN 2019gsc is marked.

found very similar to that of SN 2010ae (Stritzinger et al. 2014) at around the maximum light. SN 2019gsc exhibits a number of lines with low velocities, between 2,000–3,500  $\text{km s}^{-1}$ . In particular, the expansion velocity measured from the Si II  $\lambda$  6355 line is  $\approx 3,500 \text{ km s}^{-1}$ .

Given the relatively small number of well-observed SNe Iax in the literature (Jha 2017) and the close similarity of SN 2019gsc to the faintest members of this peculiar class of likely thermonuclear supernovae, we initiated a follow-up campaign to collect optical spectroscopic and photometric observations. Our follow-up began as soon as SN 2019gsc was classified. However, due to the low-luminosity and rapid evolution, the observing campaign was terminated just 54 d later (see Section 4.1).

Basic information of SN 2019gsc and its host galaxy is summarized in Table 1. The logbook of observations is reported in Tables 2 and 3.

## 2.1 Photometric data reduction

Optical multi-band ( $ugriz$ ) imaging of SN 2019gsc started soon after discovery and continued over the course of about fifty days, when the SN faded down to  $m_r = 22.48 \pm 0.11 \text{ mag}$ . The telescopes and instruments used for the photometric follow-up campaign are listed in Table 2.

All science images were pre-processed using standard procedures in IRAF<sup>2</sup> for bias subtraction and flat fielding. The Sloan Digital Sky Survey (SDSS; Data Release 15, Aguado et al. 2019)<sup>3</sup> stars in the field of SBS 1436+529A were used as a local photometric reference.

Accurate photometric measurements of SN 2019gsc require galaxy subtraction to isolate the SN flux contribution. We therefore used the SDSS images obtained on 2003 March 07 as templates to remove the host-galaxy contamination from each of the  $ugriz$ -band science images. The final calibrated photometry (cf. Table 2) was derived with the SNOoPY pipeline<sup>4</sup>, using the PSF-fitting technique on the template-subtracted science images and the instrumental magnitudes were then calibrated to the Sloan AB system, using Sloan stars in the field of the host galaxy.

Error estimates for the SN magnitudes are obtained through artificial star experiments in which fake stars with a similar magnitudes as the SN are placed in the fit residual image in a position close to, but not coincident with, the SN location. The simulated images are processed through the same procedure and the standard deviation of the measured magnitudes of the fake stars is taken as an estimate of the instrumental magnitude error. In practical term, this error mainly reflects uncertainty in the background subtraction. The photometry is reported in Table 2 and plotted in Fig. 2.<sup>5</sup>

The early photometric epochs of SN 2019gsc obtained by the Zwicky Transient Facility survey (Kulkarni 2018, ZTF) are also added in our analysis. Data were retrieved from the Transient Name Server (TNS)<sup>6</sup> and Lasair<sup>7</sup> (Smith, et al. 2019), listed in Table 2 and plotted in Fig. 2 as open circles. The cyan- and orange-ATLAS filters are non-standard; so the discovery and non-detection magnitudes mentioned at the beginning of Section 2 are not used in our analysis.

## 2.2 Spectroscopic data reduction

Three low-resolution optical spectra of SN 2019gsc were obtained at phases +4 d, +11 d and +54 d relative to the epoch of  $g$ -band maximum (cf. Table 3). The early two spectra were

<sup>2</sup> IRAF was distributed by the National Optical Astronomy Observatory, which is operated by the Association of Universities for Research in Astronomy (AURA) under cooperative agreement with the National Science Foundation.

<sup>3</sup> <https://www.sdss.org/dr15>

<sup>4</sup> SNOoPY is a package for SN photometry through PSF fitting and template subtraction developed by E. Cappellaro, 2014. A package description can be found at <http://sngroup.oapd.inaf.it/snoopy.html>

<sup>5</sup> Note that since only five upper limits and two epochs are available for the  $u$ - and  $z$ -bands, respectively, their values are listed in Table 2 but not included in Fig. 2.

<sup>6</sup> <https://wis-tns.weizmann.ac.il/>

<sup>7</sup> <https://lasair.roe.ac.uk/object/ZTF19aawhlcu/>

**Table 2.** Optical photometry of SN 2019gsc. Sloan *ugriz* filters (ABmag).

Date	MJD	phase <sup>a</sup>	<i>u</i> (mag)	<i>g</i> (mag)	<i>r</i> (mag)	<i>i</i> (mag)	<i>z</i> (mag)	Survey or telescope <sup>b</sup>
<b>Data from <i>Lasair</i>:</b>								
2019-05-25	58628.30	-7	...	...	>20.495	...	...	ZTF
2019-05-25	58628.22	-7	...	>20.617	...	...	...	ZTF
2019-05-29	58632.28	-3	...	...	>20.455	...	...	ZTF
2019-06-01	58635.23	0	...	19.848 (0.166)	...	...	...	ZTF
2019-06-01	58635.26	0	...	...	19.933 (0.133)	...	...	ZTF
2019-06-04	58638.20	3	...	19.922 (0.177)	...	...	...	ZTF
2019-06-04	58638.26	3	...	...	19.717 (0.123)	...	...	ZTF
2019-06-07	58641.30	6	...	...	19.737 (0.111)	...	...	ZTF
2019-06-10	58644.20	9	...	20.303 (0.287)	...	...	...	ZTF
2019-06-13	58647.25	12	...	...	19.790 (0.171)	...	...	ZTF
<b>Data from this work:</b>								
2019-06-05	58639.98	5	>19.950	19.970 (0.050)	19.673 (0.054)	19.701 (0.038)	...	LT
2019-06-06	58640.26	5	...	19.955 (0.032)	19.716 (0.050)	19.663 (0.071)	...	LCO
2019-06-08	58642.13	7	...	19.984 (0.029)	19.650 (0.016)	19.658 (0.021)	19.940 (0.047)	NOT
2019-06-08	58642.15	7	...	20.007 (0.049)	19.551 (0.043)	19.671 (0.067)	...	LCO
2019-06-08	58643.00	8	>20.292	20.175 (0.059)	19.578 (0.043)	19.673 (0.035)	...	LT
2019-06-09	58643.35	8	...	20.150 (0.400)	19.553 (0.044)	19.686 (0.073)	...	LCO
2019-06-11	58645.96	11	>20.246	20.561 (0.137)	19.750 (0.061)	19.725 (0.061)	...	LT
2019-06-12	58646.32	11	...	20.472 (0.103)	19.713 (0.076)	19.807 (0.130)	...	LCO
2019-06-15	58649.01	14	>19.283	20.715 (0.066)	20.071 (0.131)	19.863 (0.076)	...	LT
2019-06-16	58650.34	15	...	>21.068	20.151 (0.123)	19.894 (0.139)	...	LCO
2019-06-17	58651.98	17	>19.247	21.124 (0.107)	20.231 (0.144)	20.019 (0.037)	...	LT
2019-06-18	58652.24	17	...	21.140 (0.205)	20.309 (0.173)	19.964 (0.121)	...	LCO
2019-06-20	58654.21	19	...	21.438 (0.185)	20.340 (0.147)	>19.967	...	LCO
2019-06-23	58657.15	22	...	21.718 (0.229)	20.550 (0.208)	>20.264	...	LCO
2019-06-24	58658.31	23	...	22.007 (0.188)	20.779 (0.097)	20.226 (0.080)	...	LCO
2019-07-02	58666.97	32	...	>22.513	>21.496	20.665 (0.029)	20.175 (0.057)	NOT
2019-07-24	58688.90	54	...	...	22.480 (0.110)	...	...	GTC

<sup>a</sup> Phase is relative to the epoch of *g*-band maximum MJD = 58635.4.

<sup>b</sup> NOT = Nordic Optical Telescope, LT = Liverpool Telescope, LCO = Las Cumbres Observatory global network.

**Table 3.** Log of spectroscopic observations of SN 2019gsc.

Date	MJD	phase <sup>a</sup>	telescope <sup>b</sup>	range (nm)
2019-06-03	58638.97	4	NOT	350 ÷ 920
2019-06-11	58645.96	11	NOT	350 ÷ 920
2019-07-24	58688.90	54	GTC	350 ÷ 1000

<sup>a</sup> Phase is relative to the epoch of *g*-band maximum MJD = 58635.4.

<sup>b</sup> NOT = Nordic Optical Telescope, GTC = Gran Telescopio Canarias.

obtained with the 2.56-m Nordic Optical Telescope (NOT): the first one under the program 59-509 (P.I. D. Malesani), made available in TNS; the second one via NUTS2 (NOT Un-biased Transient Survey 2) collaboration<sup>8</sup> under the program 59-506 (P.I. E. Kankare et al.). The third late-time spectrum was collected with the 10.4-m Gran Telescopio Canarias (GTC), submitting a director discretionary program, DDT-GTC2019-129 (P.I. N. Elias-Rosa).

We used standard procedures and IRAF tasks for the data reduction. After bias and flat-field correction, the SN spectrum was extracted and calibrated in wavelength with

reference to standard arc lamp spectra. For the flux calibration, nightly sensitivity functions were derived from observations of spectrophotometric standard stars, used also to derive the corrections for the telluric absorption bands. A non-perfect removal of telluric absorption can affect the SN spectra, particularly at the position of the strong O<sub>2</sub> A-band located between 7590–7650 Å. Finally, the flux-calibration of each spectrum was verified against coeval broadband photometry.

### 3 LIGHT CURVE ANALYSIS

The photometric evolution of SN 2019gsc in the better sampled *gri* bands and for the first thirty days of evolution is plotted in Fig. 2. Only the *r*-band light curve shows the rise to maximum. The luminosity decline is slower at longer wavelength (*i*-band) than at shorter ones (*g*-band). By using a low-order polynomial fit to the optical *g*- and *r*-band light curves (the first *i*-band point is at maximum) we obtain the estimates of the magnitude and of the epoch of *g* and *r* maximum brightness, as well as the magnitudes reached 15 d after *g* and *r* peaks for the measure of the decline rate parameter  $\Delta m_{15}$ . Thanks to the inclusion of ZTF early-phase points, we find that SN 2019gsc reached an absolute magnitude at peak of  $M_g = -13.58 \pm 0.15$  mag ( $m_g = 19.92 \pm 0.01$  mag) on MJD

<sup>8</sup> <http://csp2.lco.cl/not/>

= 58635.4. The  $r$ -band peak occurred about 6 d later at  $M_r = -14.28 \pm 0.15$  mag ( $m_r = 19.46 \pm 0.01$  mag). The uncertainties in the absolute magnitudes are inferred propagating the errors of the fit to the peak apparent magnitudes and the errors in the adopted Galactic extinction and distance (cf. Section 2 and Table 1). The decline rates of SN 2019gsc are:  $\Delta m_{15}(g) = 1.08 \pm 0.06$  mag and  $\Delta m_{15}(r) = 0.96 \pm 0.06$  mag. In the case of normal SNe Ia this parameter is known to correlate with luminosity (Phillips 1993), while for SNe Iax the relation exhibits significant scatter (Foley et al. 2013). Positioning SN 2019gsc on the decline rate *versus* peak absolute  $r$ -band magnitude plot by Jha (2017, cf. their Fig. 2) or Magee, et al. (2016, cf. their Fig. 6), we see that the fainter type Iax SNe 2019gsc, 2008ha and 2010ae are clustered on the bottom-right of the graph, evolving faster if compared to brighter SNe Iax.

Light curve parameters for SNe 2008ha, 2010ae and 2019gsc are reported in Table 4. At peak brightness, SNe 2019gsc and 2008ha have comparable  $r$ -band magnitude (i.e.  $-14.28 \pm 0.15$  mag *vs*  $-14.25 \pm 0.14$  mag), while SN 2019gsc seems to be slightly fainter in the  $g$ -band (i.e.  $-13.58 \pm 0.15$  mag *vs*  $-13.89 \pm 0.14$  mag). These absolute magnitudes are calculated adopting  $A_V = 0.026$  mag for SN 2019gsc (cf. Section 2) and  $A_V = 0.21$  mag for SN 2008ha (as in Stritzinger et al. 2014 and in agreement with the Galactic extinction from the Schlafly & Finkbeiner 2011 recalibration of infrared-based dust maps). The estimate of the total reddening associated to SN 2010ae is uncertain. For a ‘moderate’ extinction  $E(B - V)_{\text{tot}} = 0.3$  mag which is used in this paper ( $A_B = 1.2$  mag,  $A_V = 0.9$  mag; cf. Stritzinger et al. 2014; see also Lyman et al. 2018), the  $g$ - and  $r$ -band absolute magnitudes for this supernova are  $\sim -14.2$  and  $-14.6$  mag, respectively.

The extinction-corrected,  $(g - r)_0$  and  $(r - i)_0$  intrinsic colours of SN 2019gsc are plotted in Fig. 3. For comparison, the well-sampled, intrinsic colour curves of the type Iax SNe 2008ha (Stritzinger et al. 2014), 2005hk (Phillips et al. 2007; Stritzinger et al. 2015), 2010ae (Stritzinger et al. 2014), and 2014ck (Tomasella et al. 2016) are also included. The colour-curves are corrected for the Galactic and host galaxy reddening adopting extinction values of  $A_V = 0.026$  mag (SN 2019gsc), 0.21 mag (SN 2008ha), 0.35 mag (SN 2005hk), 0.9 mag (SN 2010ae), 1.5 mag (SN 2014ck), and a standard  $R_V = 3.1$  reddening law (Cardelli, Clayton & Mathis 1989).

We obtained an estimate of the rise time of SN 2019gsc by stretching and then matching the  $r$ -band light curve to that of SN 2005hk, which has densely sampled multi-colour light curves and a very well constrained rise time to maximum (i.e.  $\approx 15$  days in the  $B$  band and  $\approx 22$  days in the  $r$  band; see Phillips et al. 2007). Thus, using a time stretching factor of about 0.7, the  $r$ -band rise time of SN 2019gsc is estimated to be  $\approx 15$  days. Alternatively, a constraint of the rise time can be obtained by fitting the early-phase light curves of the SN, if pre-maximum epochs are available, as described by Firth, et al. (2015). For SN 2019gsc the portion of the  $r$ -band light curve from pre-maximum to maximum (seven epochs, from MJD = 58635.26 to 58642.15 in Table 2) is fit with an *expanding fireball* model  $f_{\text{model}}(t) = \alpha(t - t_0)^n$ , with  $n = 2$  (Riess et al. 1999), similarly to what was done for SN 2014ck (Tomasella et al. 2016). From our polynomial best-fit to the early light curve of SN 2019gsc, we obtain  $t_0 = 58626^{+3}_{-5}$  MJD as the time of the first light. The reported uncertainty corresponds to the standard deviation of

the  $t_0$  parameter when fitting a range of power laws, having  $1.8 \leq n \leq 2.2$ , to the pre-maximum  $r$ -band light curve, as the analysis of large SN samples are found to be consistent with that spread of the  $n$  index (Piro & Nakar 2014). Consequently, SN 2019gsc has an  $r$ -band rise time  $t = 16^{+3}_{-5}$  d, and a  $g$ -band rise time  $\approx 10$  days ( $10^{+3}_{-5}$  d), applying the  $\sim 6$  days lag between  $g$  and  $r$  maximum. This is consistent to the value inferred by using the 0.7 stretching factor. In the following, we adopt 10 days as the rise time of the bolometric light curve of SN 2019gsc (with  $\sim 40\%$  uncertainty), considering our  $g$ -band rise and the  $\Delta t_{\text{rise}}$  of bolometric *vs.* filtered data (cf. Firth, et al. 2015, their Table 2).

### 3.1 Bolometric light curve and energetics

Using the *gri*-band photometry of SN 2019gsc, we construct the pseudo-bolometric light curve in Fig. 4. The photometry obtained at each epoch was converted to flux at the effective wavelength of its corresponding passband. If photometry was not available in a given filter on a particular night, a magnitude was estimated through interpolation between adjacent epochs, or if necessary, by extrapolation assuming a constant colour from the closest available epochs. The fluxes were then corrected for reddening, yielding the spectral energy distribution (SED) at each epoch. These SEDs were integrated using a trapezoidal integration algorithm, assuming zero flux at the integration boundaries. Finally, the flux at each epoch was converted to luminosities using our adopted distance to the host galaxy (see Table 1).

For comparison, the bolometric light curves of the faint SNe 2008ha and 2010ae, the intermediate SN 2014ck, and the bright SN 2012Z, are also plotted in Fig. 4. The light curves of the comparison objects are computed following the same prescription adopted for SN 2019gsc, making use of the available photometry, reddening values (also reported above, cf. Section 3), and distances found in the literature, i.e.: (i)  $E(B - V)_{\text{tot}} = 0.11$  mag,  $\mu = 32.59$  mag and *uBVgri*-bands for SN 2012Z (plus few *YJH* late-epoch data), from Stritzinger et al. 2015; (ii)  $E(B - V)_{\text{tot}} = 0.5$  mag,  $\mu = 31.94$  mag and *uBVgrizJHK*-bands for SN 2014ck, from Tomasella et al. 2016; (iii)  $E(B - V)_{\text{tot}} = 0.07$  mag,  $\mu = 31.55$  mag and *uBVgriYJH*-bands for SN 2008ha, from Stritzinger et al. 2014; (iv)  $E(B - V)_{\text{tot}} = 0.3$  mag,  $\mu = 30.58$  mag and *BVgrizYJH*-bands for SN 2010ae, from Stritzinger et al. 2014; Lyman et al. 2018; (with  $H_0 \equiv 73$  km s $^{-1}$  Mpc $^{-1}$ ). Unfortunately, no ultraviolet (UV) nor near-IR (NIR) observations of SN 2019gsc were taken, and only a few *u*-band upper-limits were collected during our follow-up campaign. An estimation about the *uB*- and NIR-bands contribution to the light curve of SN 2019gsc is inferred from the ratio in flux between the Optical-to-Infrared (OIR, i.e. using all the available *uBVgriYJH*-bands), and the optical (*gri*-bands only) bolometric light curves of SN 2008ha. The result is visually highlighted in the inset of Fig. 4: the *gri* light curves of SNe 2019gsc and 2008ha are almost overlapping, showing peak luminosity  $L_{19\text{gsc},\text{gri}} = 5.5 \pm 0.9 \times 10^{40}$  erg s $^{-1}$  and  $L_{08\text{ha},\text{gri}} = 5.7 \pm 0.5 \times 10^{40}$  erg s $^{-1}$ , respectively. Thus we suppose that SN 2019gsc should have an OIR bolometric light curve very similar to the model fit of SN 2008ha, which is plotted as a solid line in Fig. 4 (peak luminosity  $L_{08\text{ha},\text{OIR}} \approx 1.12 \times 10^{41}$  erg s $^{-1}$ ); i.e., apply-

ing a percentage increase by approximately 96%, we derive  $L_{19\text{gsc, OIR}} \approx 1.08 \pm 0.1 \times 10^{41}$  erg s $^{-1}$ . The  $u$ -band alone contributes to  $\sim 10\%$  at maximum (dropping to 1-2% few days later); overall the bluest bands ( $uBV$ ) account for most of the increase of the peak luminosity, while the NIR-bands ( $YJH$ ) contribute  $\sim 10 \div 15\%$ . This is roughly quantified comparing the fluxes of different pseudo-bolometric light curves of SN 2008ha, constructed including or excluding several photometric bands. The relevance of the NIR contribution to the late-phase bolometric light curve of SN 2012Z is also highlighted in Fig. 4, where the OIR ( $uBVgriYJH$ ) bolometric light curve is over-plotted as a dotted line to the optical ( $uBVgri$ ) one (yellow triangles). For what concern the ultraviolet (UV) contribution, we note that SNe 2005hk and 2012Z were detected in the UV at very early phases, but they both faded below the detection limit well before the epoch of optical maximum (Phillips et al. 2007; Brown et al. 2009; Stritzinger et al. 2015). This implies that, in both objects, the flux in the UV drops well below 10% of the total flux before maximum. In general, SNe Iax are bluer than normal SNe Ia in the UV before maximum light, but quickly redden (by  $\sim 1.5 - 2$  mag in *Swift*  $uvw1-b$ ). Hence,  $\sim 10$  days post maximum, they are already redder than normal SNe Ia (Jha 2017).

With the assumption that the light curve of SN 2019gsc is powered by  $^{56}\text{Ni}$  decay, the amount of  $^{56}\text{Ni}$  synthesized during the explosion is estimated using Arnett’s rule (Arnett 1982). See Stritzinger & Leibundgut (2005), their Section 4, for an analytical expression that links  $^{56}\text{Ni}$  mass to the peak bolometric luminosity. Adopting  $10 \pm 4$  days rise time on the bolometric output of SN 2019gsc and  $\approx 11 \pm 1 \times 10^{40}$  erg s $^{-1}$  for the peak luminosity, with the assumptions described in Arnett (1982), we obtain the crude estimate of  $M_{\text{Ni}} \approx 0.003 \pm 0.001 M_{\odot}$ . The relative error on  $M_{\text{Ni}}$  is found by adding the relative errors on the peak luminosity (i.e. 0.10, which in turn depends on the accuracy of the adopted distance and reddening), and on the energy input from the decay of  $^{56}\text{Ni}$  (i.e. 0.29; which is due to the error on the rise time).

Compared to normal SNe Ia and to the prototype SN 2002cx, the low expansion velocity of the SN 2019gsc ejecta ( $v_{\text{ejc}} \approx 3.5 \times 10^3$  km s $^{-1}$ , cf. Section 4 and Fig. 8) suggests it also has much lower ejecta mass ( $M_{\text{ej}}$ ) and kinetic energy ( $E_k$ ). Quantitatively, the explosion parameters providing a good match to the bolometric light curve of SN 2019gsc are  $M_{\text{ej}} \approx 0.13 M_{\odot}$  and  $E_k \approx 12 \times 10^{48}$  erg, using Arnett’s equations Arnett 1982 as done in Valenti et al. 2009 and Foley et al. 2009 for SN 2008ha. The energetics are similar to those inferred for both SN 2008ha and SN 2010ae. With regard to the reliability of the above estimations of ejecta mass and kinetic energy, we underline that the model relies upon a number of simplifying assumptions including: complete energy deposition supplied from the radioactive  $^{56}\text{Ni}$  decay, no appreciable mixing of  $^{56}\text{Ni}$ , spherical symmetry and homologous expansion of the ejecta. Finally the model also relies on a constant optical opacity of about 0.1 cm $^2$  g $^{-1}$ . It is well known that opacity has a strong dependence on the temperature and therefore a strong time dependence (Hoeftlich, Khokhlov & Mueller 1992). With these assumptions in mind, Arnett’s rule is accurate to within  $\sim 50\%$  (Stritzinger et al. 2015).

**Table 4.** Light curves parameters for SN 2019gsc (this work), SN 2008ha, and SN 2010ae (from Stritzinger et al. 2014). The absolute magnitudes for SNe 2019gsc, 2010ae and 2008ha are derived using  $A_V = 0.026, 0.90$  and  $0.21$  mag, respectively.

Filter	$m_{\text{peak}}$ (mag)	$M_{\text{peak}}$ (mag)	$\Delta m_{15}$ (mag)
<b>SN 2019gsc</b>			
$g$	$19.92 \pm 0.01$	$-13.58 \pm 0.15$	$1.08 \pm 0.06$
$r$	$19.46 \pm 0.01$	$-14.28 \pm 0.15$	$0.96 \pm 0.06$
<b>SN 2010ae</b>			
$g$	$17.49 \pm 0.02$	$-14.2 \pm 0.5$	$1.51 \pm 0.05$
$r$	$16.92 \pm 0.02$	$-14.6 \pm 0.5$	$1.01 \pm 0.03$
<b>SN 2008ha</b>			
$g$	$17.97 \pm 0.02$	$-13.89 \pm 0.14$	$1.80 \pm 0.03$
$r$	$17.57 \pm 0.01$	$-14.25 \pm 0.14$	$1.11 \pm 0.04$

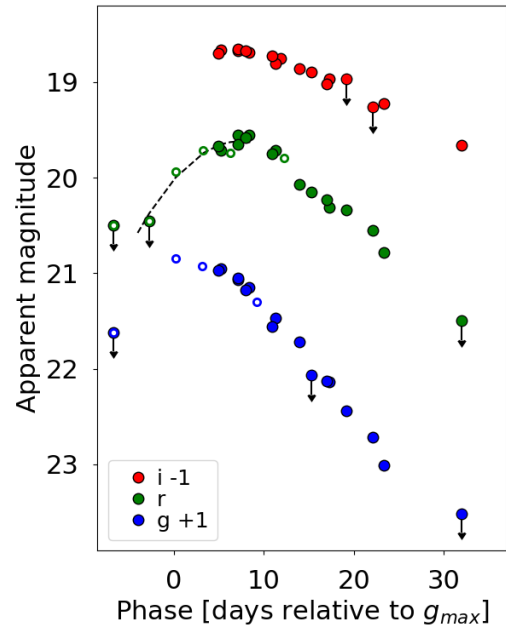


**Figure 2.** Optical  $gri$ -bands light curves of SN 2019gsc in the AB system. For clarity, the light curves have been shifted vertically as indicated in the legend. The open circles correspond to photometric points taken from the ZTF archive (cf. Table 2). Epochs with arrows are upper-limits. The early portion of the  $r$ -band light curve is fitted with an *expanding fireball model*, with  $n = 2$  (cf. Section 3).

## 4 SPECTROSCOPIC ANALYSIS

Our spectroscopic time series of SN 2019gsc consists of three optical spectra, distributed over fifty days. The last spectrum was taken when the object had faded to a magnitude of  $m_r = 22.48 \pm 0.11$  mag. The spectroscopic sequence is shown in Fig. 5.

The first spectrum taken at maximum light exhibits a blue continuum (the blackbody temperature is  $T_{bb} \approx 9 \times 10^3$  K, cf. Fig. 8) superposed with a rich structure, along with several low-velocity P Cygni features associated with both intermediate-mass elements (IMEs) and Fe-group el-

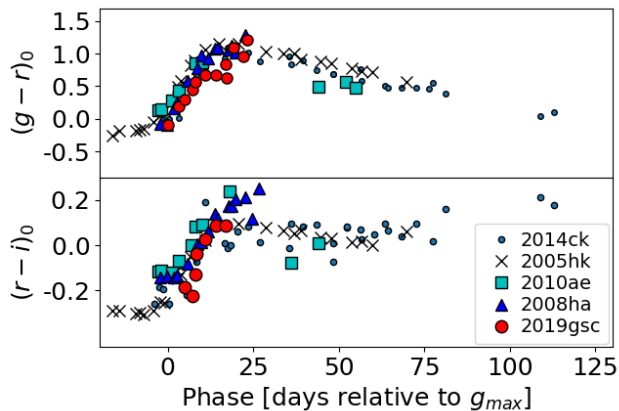


**Figure 3.** Extinction-corrected colour curves of SN 2019gsc compared with those of SNe 2008ha, 2010ae, and 2005hk (Stritzinger et al. 2014, 2015), and SN 2014ck (Tomasella et al. 2016).

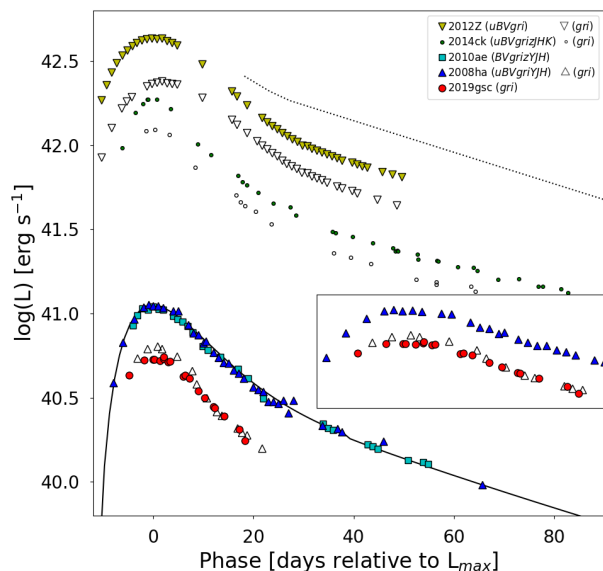


**Figure 4.** Pseudo-bolometric light curve of SN 2019gsc constructed by integrating over the *gri*-band flux points. The pseudo-bolometric light curves of SNe 2012Z (yellow triangles: *uBVgri*-bands; open triangles: *gri*-bands), 2014ck (green circles: *uBVgrizJHK*-bands; open circles: *gri*-bands), 2010ae (*BVgrizYJH*-bands), 2008ha (blue triangles: *uBVgriYJH*-bands; open triangles: *gri*-bands) are also plotted for comparison. The model fit of the SN 2008ha light curve is over-plotted as a solid line. The dotted line represents the SN 2012Z light curve with the inclusion of NIR photometry (see text for details). The inset shows a zoomed view around maximum of the pseudo-bolometric light curve of SN 2019gsc (red circles), compared with those of SN 2008ha constructed either including all the available *uBVgriYJH*-bands (blue triangles), or only the optical *gri*-bands (open triangles).

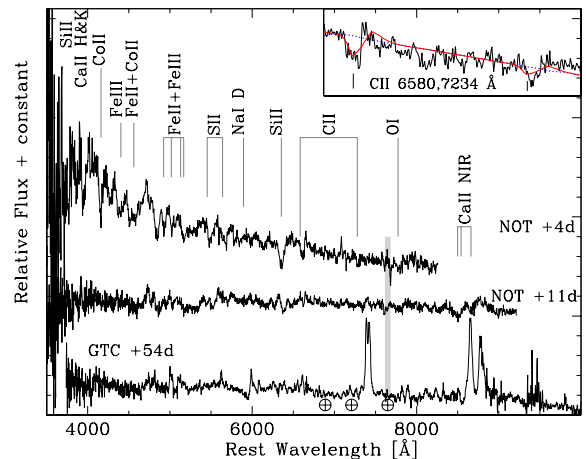


**Figure 5.** Spectroscopic sequence of SN 2019gsc, along with line identification of prominent features. The inset on the top shows the region of the +4d spectrum (black) centered on C II  $\lambda\lambda 6580, 7234$ , with the SYNOW synthetic spectra of the C II (solid red line) and Fe II ions (dotted blue) overplotted.

ements. By comparison with normal SNe Ia and using the SYNOW (Branch et al. 2004) spectral synthesis code for fitting our spectra with profiles of various ions, we identify: a relatively weak and narrow Si II  $\lambda 6355$  feature, along with absorptions attributed to Ca II H&K and Ca II NIR triplet; Si II  $\lambda\lambda 5454, 5640$ ; Na I D; O I  $\lambda 7774$  (which is visible from day +1 to +52); high-excitation lines of Fe II, Co II and Fe III, which appear to produce most of the observed features blueward of  $\sim 5000$  Å; and, possibly, C II  $\lambda\lambda 6580, 7234$ . There is some indication that early spectra of type Ia SNe contain C II and, sometimes, also C III (i.e. Chornock, et al. 2006; Foley et al. 2013; Tomasella et al. 2016). Actually, we obtain a reasonable fit to absorption features at  $\sim 6580$  and  $7230$  Å adding the C II ion in the SYNOW spectral model (rather than other ions, i.e. Fe II), as it is shown in the inset of Fig. 5. If this identification is correct, the detection of C II in the ejecta of SN 2019gsc might be related to unburnt material of the progenitor system, giving indication on its nature (C/O WD vs O/Ne/Mg WD; see Nomoto, Kamiya & Nakasato 2013), or on the mechanism by which the explosive flame propagates throughout the WD (Folatelli et al. 2012).

In Fig. 6 the spectra of SN 2019gsc are compared with those of the fast-and-faint type Ia SNe 2008ha and 2010ae at similar phases. Notably, all spectra are very similar at maximum light and one week later, while about fifty days after maximum, forbidden calcium emission lines are strong in SNe 2019gsc and 2008ha, while in SN 2010ae they are relatively weak and emerge only during later epochs (see Section 4.1).

#### 4.0.1 Search for helium in +11 day spectrum

Several authors (i.e. Filippenko et al. 2007; Foley et al. 2013, 2016; Magee et al. 2019; Jacobson-Galán et al. 2019) have investigated the prospect to detect helium features in SNe Ia spectra, following the notion that their progenitor are C/O (or hybrid C/O/Ne) WDs accreting material

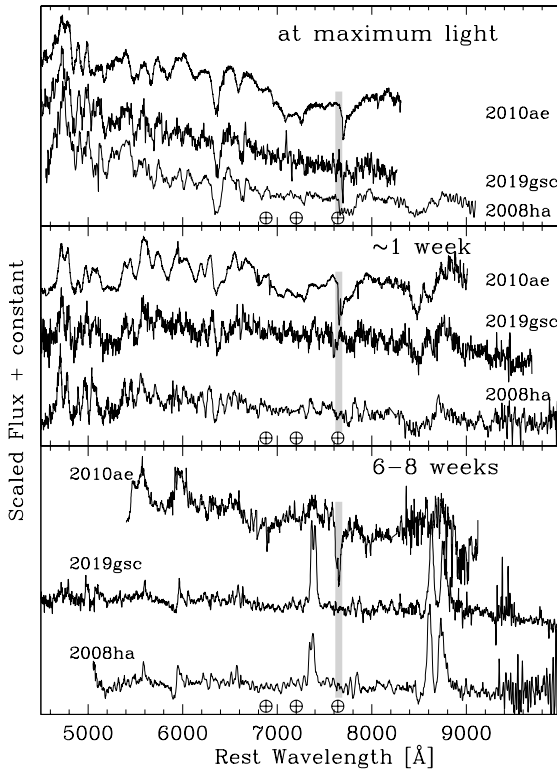


**Figure 6.** Sequences of spectra of the faint type Iax SNe 2019gsc, 2010ae, and 2008ha at similar phases, extending from around maximum light, to one week, and finally out to 6 ÷ 8 weeks post maximum. The spectra of SN 2008ha are from [Valenti et al. \(2009\)](#) and those of SN 2010ae from [Stritzinger et al. \(2014\)](#).

from a helium star companion. [Foley et al. \(2013\)](#) identified two SNe Iax with clear He I lines in their post-maximum spectra, i.e. SN 2004cs and SN 2007J (cf. their Section 5.2 and Figure 22). They roughly estimate that  $\sim 15\%$  of SNe Iax can exhibit helium signatures during a specific phase of their spectroscopic evolution. [Magee et al. \(2019\)](#) presented a series of simulations with varying helium abundances, calculated using the TARDIS radiative transfer code ([Kerzendorf & Sim 2014](#)) and based on the multi-dimensional explosion models of [Kromer et al. \(2015\)](#). They show that the best chance for detecting He I features is either at NIR wavelengths (with He I  $\lambda 10830$  being the strongest line) or in the post-maximum spectra of the faintest members of the class. Therefore, the extremely faint SN 2019gsc offers an excellent opportunity to search for signatures of helium, although our spectral coverage includes only the optical helium lines (i.e. He I  $\lambda 5876$ ,  $\lambda 6678$ ,  $\lambda 7065$ ).

In Fig. 7 we compare our +11 d optical spectrum of SN 2019gsc with the synthetic N5def-hybrid models calculated by [Magee et al. \(2019\)](#) specifically for the faintest members of the SN Iax class at +15 d after bolometric maximum light. As in [Magee et al. \(2019\)](#), spectra have been normalised to the median flux in the wavelength range 5000 Å

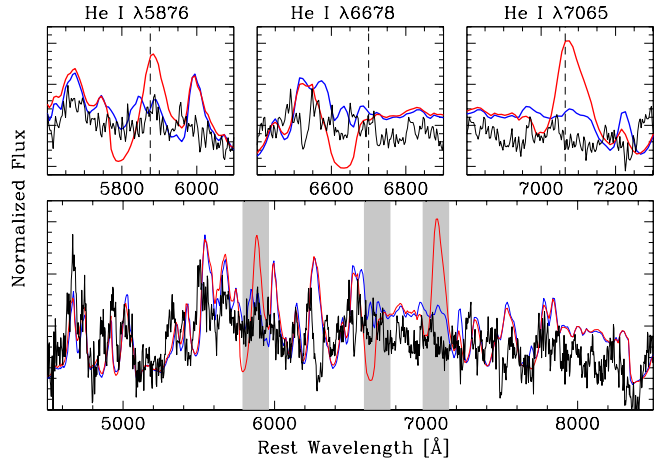


**Figure 7.** Comparison of the +11 d spectrum of SN 2019gsc with the N5def-hybrid models by [Magee et al. \(2019\)](#) with 0.22% (blue line) and 36% (red line) helium abundances. On top, from left to the right the panels show the wavelength regions of He I  $\lambda 5876$ ,  $\lambda 6678$  and  $\lambda 7065$ , respectively (highlighted with shaded grey bars on the bottom panel). Spectra have been normalised to the median flux in the wavelength range 5000 Å – 7000 Å

– 7000 Å. Only a marginal evidence of helium, if any, can be advanced for SN 2019gsc. The best match is with the N5def-hybrid model (blue line in Fig. 7) which has a low helium abundance (0.22% of the ejecta mass). We note that the N5def-hybrid ejecta mass ( $0.014 M_{\odot}$ ; [Kromer et al. 2015](#)) is by an order of magnitude lower than the one estimated for SN 2019gsc ( $0.13 M_{\odot}$ ; see Section 3.1). Hence, we speculate that SN 2019gsc could contain a few  $10^{-4} M_{\odot}$  of helium at most.

#### 4.0.2 Expansion velocities of the ejecta

The low expansion velocity of the ejected material is a hallmark of SNe Iax and is indicative of a low kinetic energy in comparison to normal SNe Ia explosions, as previously noted in Sect. 3.1. The ejecta velocity of SN 2019gsc is estimated from the location of the absorption minimum of Si II  $\lambda 6355$ , which suffers negligible line blending relative to other features in the spectrum. We measure a Si II expansion velocity of  $v_{ejc} \approx 3,500 \text{ km s}^{-1}$  at the time of g-band maximum and this decreases to  $v_{ejc} \approx 2,400 \text{ km s}^{-1}$  about ten days later. In Fig. 8 (bottom panel) the expansion velocity evolution of the three faintest SNe Iax, SNe 2008ha, 2010ae, and 2019gsc, is compared with the prototypical type Iax SN 2002cx. We conclude that the expansion velocities of SN 2019gsc are similar to those of SN 2008ha, and about  $\sim 20\%$  and  $\sim 40\%$  lower than in SN 2010ae and SN 2002cx, respectively.

Taking the Si II  $\lambda 6355$  absorption line as an indicator of the expansion velocity, the ratio between the Doppler velocity of the putative C II  $\lambda 6580$  and Si II  $\lambda 6355$  at maximum is  $\sim 0.5$  (cf. Fig. 8), which is similar to that observed in SN 2008ha ([Parrent et al. 2011](#)). This ratio is generally slightly above unity in normal SNe Ia ([Folatelli et al. 2012](#));  $\sim 0.89$  and  $\sim 0.95$  in SN 2012Z and SN 2014ck, respectively ([Stritzinger et al. 2015](#); [Tomasella et al. 2016](#)). The fact that the C II Doppler velocity is significantly lower than the ex-



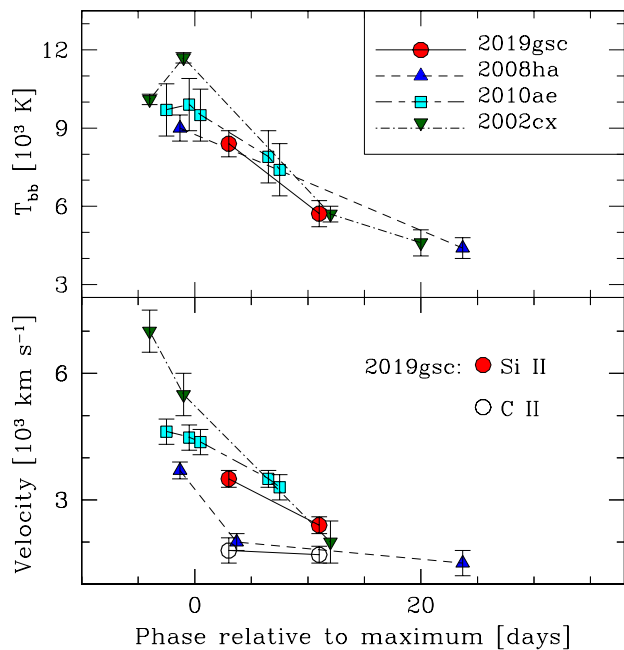


**Figure 8.** Top-panel: comparison of the time evolution of  $T_{bb}$  for SN 2019gsc with SNe 2008ha, 2010ae and 2002cx. Bottom-panel: expansion velocity evolution of the ejecta of SN 2019gsc, estimated measuring the location of the absorption minimum of Si II  $\lambda 6355$  (filled red circles) and C II  $\lambda 6580$  (open circles). Si II  $\lambda 6355$  velocity for SN 2008ha (filled blue triangles), SN 2010ae (filled cyan squares) and SN 2002cx (filled green triangles) are also reported.

expansion velocity may indicate ejecta asymmetries as suggested by Foley et al. (2016) for SN 2008ha, or alternatively the line is not associated with C II. In passing, we note that the C II line velocity is considerably lower than Si II velocity also for the peculiar 09dc-like SNe (Taubenberger 2017; Taubenberger, et al. 2019, see their Fig. 8).

Also plotted in Fig. 8 (top panel) are the rough estimates of the photospheric temperature of SN 2019gsc as derived from a blackbody (BB) function fit to the spectral continuum. Only the first two epochs were considered, as at +54 d the presence of emission lines and line blanketing drive a flux deficit at shorter wavelengths. Spectra were corrected for redshift and extinction before the fit. Errors are estimated from the dispersion of measurements obtained with different choices for the spectral fitting regions. The photospheric temperature of SN 2019gsc at maximum is around 8,000 K to 9,000 K, rapidly decreasing below 6,000 K one week later, similar to the BB temperature evolution of SNe 2008ha and 2010ae.

#### 4.1 The Gran Telescopio Canarias late-time spectrum

We observed SN 2019gsc with the Gran Telescopio Canarias (GTC) equipped with OSIRIS and using the R1000B+R1000R grisms. This setup provided wavelength coverage from 363.0 nm to 1000 nm. The observations were carried out on 2019 July 24, when the SN was +54 d post-

maximum and its brightness had faded to  $m_r = 22.48 \pm 0.11$  mag (as measured in the acquisition images), with a total integration time of 2 hours.

The high-quality GTC spectrum of SN 2019gsc exhibits the late-time spectral characteristic of the SN Iax class, consisting of a weak continuum, or pseudo-continuum, superposed with both permitted and forbidden emission lines (Foley et al. 2016). The best match is with the faint type Iax SN 2008ha at a similar phase (cf. Fig. 9, top-left panel).

As shown in Fig. 9, the late-time spectrum of SN 2019gsc is also similar to that of the brighter type Iax SN 2014ck (peak  $M_V \approx -17.29$  mag, Tomasella et al. 2016) taken at a phase of +166.3 d, thus highlighting the very rapid spectroscopic evolution of the fainter members of the SN Iax class.

Following Li et al. (2003); Jha et al. (2006); Sahu et al. (2008), we tentatively identify narrow, permitted Fe II features and a number of forbidden lines associated to iron, cobalt and calcium (see Fig. 9). Several lines blueward of  $\sim 6000$  Å can be a blend of permitted Fe II features, which are identified at earlier epochs with higher velocities. Iron lines can be present also between 6200 and 6600 Å, as highlighted by Jha et al. (2006) and Sahu et al. (2008) for type Iax SNe 2002cx and 2005hk, respectively.

The strongest features are attributed to calcium, including both the Ca II NIR triplet and the forbidden [Ca II]  $\lambda\lambda 7292, 7324$  doublet, having a full-width-half-maximum (FWHM) velocity of 1400 and 1500 km s<sup>-1</sup>, respectively. Both permitted and forbidden calcium lines are significantly more prominent in SN 2019gsc than SN 2002cx taken at a similar phase, and are comparable to those of SN 2008ha.

As for SNe 2002cx (Jha et al. 2006) and 2005hk (Sahu et al. 2008), several weak O I lines are tentatively recognized in SN 2019gsc until late phases (see Fig. 9, bottom-panel), suggesting that the elements in the ejecta are homogeneously mixed. In contrast, forbidden oxygen features [O I]  $\lambda\lambda 6300, 6364$  are not detected in this late-time spectrum of SN 2019gsc (so far [O I] has never been observed in SNe Iax, cf. Jha et al. 2006; McCully et al. 2014; Foley et al. 2016). It was suggested that [Ca II]  $\lambda\lambda 7292, 7324$  can limit the strength of [O I]  $\lambda\lambda 6300, 6364$  emission from a region in which both these ions co-exist (Dessart & Hillier 2015, and references therein). In passing, we note that normal stripped-envelope, core-collapse SNe exhibit strong [O I] emission at late times. The absence of forbidden oxygen in the late-time spectra of SNe Iax weakens the link with core-collapse SNe which have been also considered a possible explanation for SNe Iax (Valenti et al. 2009; Moriya et al. 2010).

To summarise, we find that the +54 d spectrum of SN 2019gsc is similar to those of other SNe Iax at least half a year post maximum. This is an exceptionally fast spectral evolution, similar to SN 2008ha, but not to SN 2010ae (Stritzinger et al. 2014), which does not exhibit forbidden Ca II emission at the same phase (cf. Fig. 9).

## 5 ENVIRONMENTS OF FAINT TYPE IAX SNE

SNe Iax are usually found in star-forming, late-type host galaxies. Lyman et al. (2018) have recently performed spec-

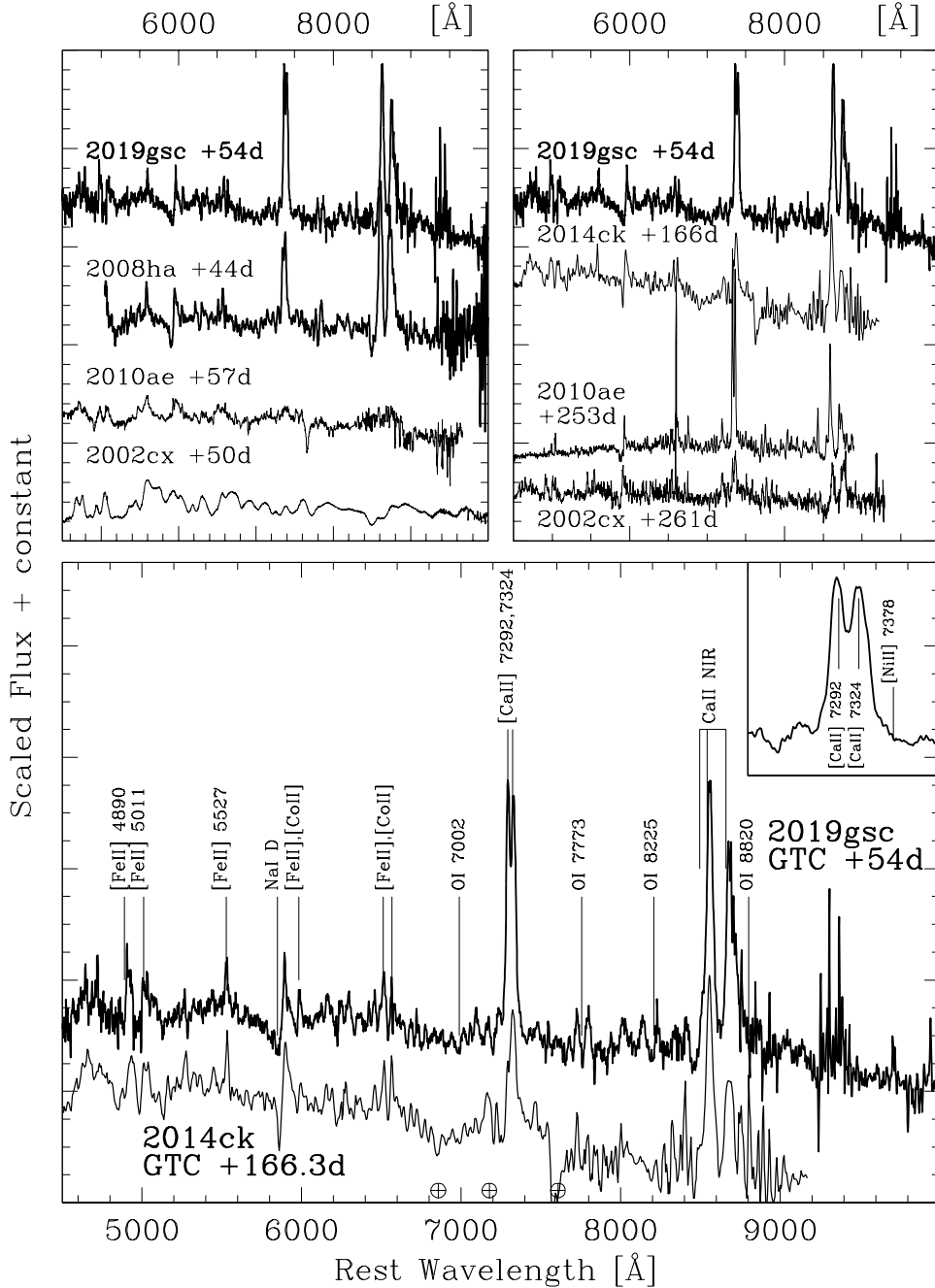


**Figure 9.** Top-left panel: comparison of the +54 d GTC spectrum of SN 2019gsc with similar phase spectra of SN 2008ha (Valenti et al. 2009), SN 2010ae (Stritzinger et al. 2014), and the prototype of the class SN 2002cx (Li et al. 2003). Top-right panel: the same spectrum of SN 2019gsc is compared with the spectra of the brighter type Ia SN 2014ck (Tomasella et al. 2016) and SN 2002cx, and with the faint SN 2010ae, taken at phases > 5 months. Bottom-panel: zoomed-view of the GTC late-spectrum of SN 2019gsc, with tentative identification of the principal forbidden lines, based on Li et al. 2003. Permitted Ca II and O I lines (showing P Cygni profiles) are also reported, while several Fe II features (which are too numerous to be included) are superimposed on a pseudo-continuum, according to late-time spectral modelling of type Ia SNe 2002cx and 2005hk by Jha et al. 2006 and Sahu et al. 2008, respectively. The inset shows the region centered on [Ca II]  $\lambda\lambda$ 7292, 7324 doublet. The position of (weak/absent) [Ni II]  $\lambda$  7378 is marked.

**Table 5.** Estimates for SN 2019gsc host-galaxy and explosion-site oxygen abundance  $12 + \log_{10}(\text{O}/\text{H})$ , using the calibration for  $O3N2$  by Marino et al. (2013).

host galaxy nucleus	$8.10 \pm 0.18$ dex
SN site 1	$8.23 \pm 0.18$ dex
SN site 2	$8.17 \pm 0.18$ dex

troscopic environmental measurements of the host galaxies and the explosion sites for about twenty SNe Iax (see their Table 1). They find that the metallicity distribution of the SNe Iax explosion site is similar to that of core-collapse SNe, and metal poor in comparison to normal SNe Ia as well as spectroscopically classified 1999T-like objects. Moreover, fainter members of the SN Iax class are found to be located in very metal poor environments. However, their sample contains a small number of very faint objects and consequently the statistics are limited. New SNe Iax are crucial to gain further information on this topic, and, in this respect, the extremely-faint SN 2019gsc is particular interesting.

In order to derive the metallicity for the host galaxy of SN 2019gsc and for its explosion site, we use spectra downloaded from SDSS DR12 as well as our own GTC spectrum (cf. Sect. 4.1), and the calibration of Pettini & Pagel (2004) or Marino et al. (2013). These authors calibrate the oxygen abundances of extra-galactic H II regions for which the oxygen abundance was determined with the direct  $T_e$ -based method against the  $N2$  and  $O3N2$  indices:  $N2 \equiv \log_{10}([\text{N II}]\lambda 6583/\text{H}\alpha)$  and  $O3N2 \equiv \log_{10}([\text{O III}]\lambda 5007/\text{H}\beta)/([\text{N II}]\lambda 6583/\text{H}\alpha)$ . The  $N2$  and  $O3N2$  indices have advantage over other types of calibrations in the literature due to the small wavelength separation between the lines, and hence are less sensitive to the extinction and to issues related to flux calibration.

When using the archive spectra of SBS 1436 + 529A, the emission line flux measurement (as described in Lyman et al. 2018, their Section 3.3), provides the indices  $N2 = -1.43 \pm 0.03$  and  $O3N2 = 2.04 \pm 0.04$ . Thus, we estimate the SN 2019gsc host-galaxy oxygen abundance to be: (i)  $12 + \log_{10}(\text{O}/\text{H}) = 8.08 \pm 0.01$  dex, using the calibration for  $O3N2$  of Pettini & Pagel (2004); or (ii)  $12 + \log_{10}(\text{O}/\text{H}) = 8.10 \pm 0.01$  dex, using the calibration for  $O3N2$  of Marino et al. (2013). The reported errors are formal errors. Added in quadrature with systematic errors related to determining the gas-phase metallicity, i.e.,  $\approx 0.16 - 0.18$  dex (Marino et al. 2013), we obtain  $12 + \log_{10}(\text{O}/\text{H}) = 8.10 \pm 0.18$  dex (using the  $O3N2$  calibration by Marino et al. 2013; similar values, within the error, come from the  $N2$  index and/or Pettini & Pagel 2004 calibration). This value is sub-solar (using  $12 + \log_{10}(\text{O}/\text{H}) = 8.69$  dex as the solar abundances, see Asplund et al. 2009).

As our GTC long-exposure (2 hours), long-slit spectrum includes also the bright H II regions both on the left and on the right of the position of the SN location (see Fig. 10), we extracted a 1-D spectrum for each H II region. Thus, we derive also the oxygen abundance for the H II regions close to the SN 2019gsc explosion site using the individual line fluxes, in the same manner as done with the host-galaxy spectrum. We report the results in Tab. 5 and note that they too suggest a sub-solar ‘metallicity’. All three of our oxygen abundance estimates are in agreement within the errors.

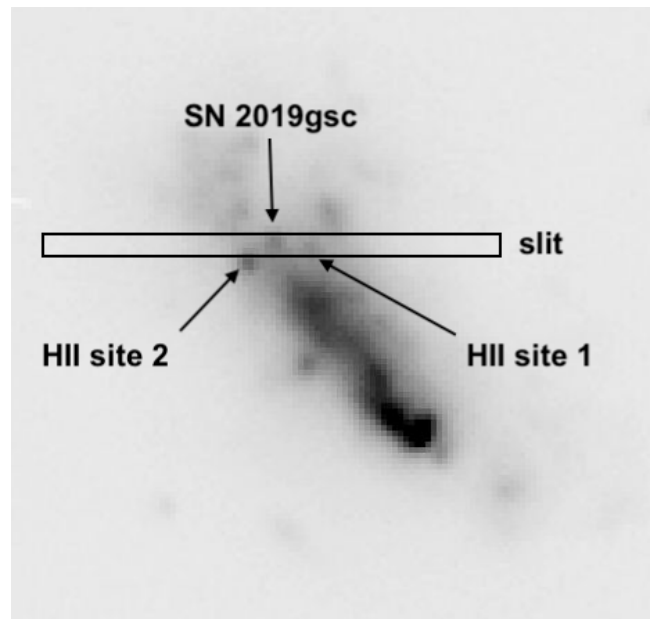


**Figure 10.** Slit position during the acquisition of the GTC spectrum of SN 2019gsc. Bright H II regions on the right (site 1) and on the left (site 2) of the SN were also captured.

These measurements place SN 2019gsc on the metal-poor tail of the oxygen abundances distribution for the SN Iax collection by Lyman et al. (2018, cf. their Table 4). The metallicity of the host galaxy of SN 2019gsc is lower than those of all SN Iax host galaxies in the Lyman et al. (2018) sample, both for the SN explosion site and the host nucleus. It is very similar to the metallicity deduced from the explosion site of SN 2008ha, i.e.  $8.22 \pm 0.18$  dex.

As a test case, we also downloaded the host spectrum of SN 2010ae, ESO 162-017 (from 6DF Galaxy Survey, via NED<sup>9</sup>), and the estimation of the oxygen abundance is  $8.32 \pm 0.18$  dex, using the  $O3N2$  index and Marino et al. (2013) calibration. This is in full agreement with the value of  $8.34 \pm 0.14$  dex measured by Stritzinger et al. (2014) and  $8.31 \pm 0.18$  dex by Lyman et al. (2018).

## 6 CONCLUSIONS

The observations presented in this paper provide a view on an extreme member of the class of faint-and-fast evolving SNe Iax that includes SN 2008ha, SN 2010ae, and even SN 2009J (Foley et al. 2013). SN 2019gsc is characterized by an extremely low luminosity, reaching an absolute peak  $g$ -band magnitude of only  $M_g = -13.58 \pm 0.15$  mag ( $M_g = -13.89 \pm 0.14$  mag for SN 2008ha), displays a decline rate of about  $\Delta m_{15}(g) = 1.08 \pm 0.06$ , and a  $g$ -band rise time of  $\approx 10^{+3}_{-5}$  d. It also exhibits a low expansion velocity of the ejecta, about  $\sim 3,000$  km s<sup>-1</sup> at maximum, and consequently low kinetic energy, similar to SN 2008ha. The peaks of the pseudo-bolometric light curves indicate that SNe 2008ha, 2010ae and 2019gsc produced around a

<sup>9</sup> <http://www.6dfgs.net/>

few  $\times 10^{-3} M_{\odot}$  of  $^{56}\text{Ni}$ . We report the simultaneous publication of observational data on SN 2019gsc by [Srivastav, et al. \(2020\)](#). They find peak absolute magnitudes, decline rate (i.e.  $M_g = -13.75 \pm 0.23$  mag;  $M_r = -13.97 \pm 0.16$  mag;  $\Delta m_{15}(r) = 0.91 \pm 0.1$  mag), and explosion parameters which are compatible, within the errors, with ours.

In many ways, SN 2019gsc is a clone of the exceptional and still enigmatic SN 2008ha ([Foley et al. 2016](#)). Thus, it enters in the debate concerning the nature and origins of these events: core-collapse or thermonuclear explosions? ([Valenti et al. 2009](#); [Foley et al. 2009](#); [Moriya et al. 2010](#); [Foley et al. 2016](#)). Recently, there have been some explorations of explosion scenarios that can produce rapidly-evolving faint transients, even fainter than the faintest SNe Iax. These include the outcomes of stripped-envelope electron-capture SNe (ECSNe, [Moriya & Eldridge 2016](#)), as well as a double-degenerate scenario consisting of the merger of a C/O and a O/Ne WD ([Kashyap et al. 2018](#)). However, to date no spectral modelling for ECSNe ([Moriya & Eldridge 2016](#)) is available and the published synthetic light curves do not cover a wide range in peak luminosity. Moreover, while the light curve properties and ejecta velocities of the faintest SNe Iax may appear to be somewhat consistent with the stripped-envelope ECSNe model, we stress that the post maximum NIR spectroscopic sequence, obtained by [Stritzinger et al. \(2014\)](#) for SN 2010ae as well as for the brighter SN 2014ck in [Tomasella et al. \(2016\)](#) and, earlier, for SN 2005hk in [Kromer et al. \(2013\)](#), indicates the presence of Co II and hence provides a stronger link to thermonuclear explosions. Despite the lack of NIR spectra for SN 2019gsc, as well as for SN 2008ha, the striking spectral similarities in the visual-wavelength range with both the faint SN 2010ae, and the brighter SNe 2002cx and 2014ck (when comparing spectra at different epochs, cf. Fig. 9), suggest a similar explosion mechanism for the broad class of SNe Iax.

We stress that the spectroscopic evolution of SN 2019gsc is unusually rapid, as strong forbidden iron and calcium emission lines have clearly emerged in the spectrum taken on +54 d. Equally strong at this epoch are the permitted Ca II NIR triplet features. Our late-time spectrum perfectly matches the similar-phase (+44 d) spectrum of SN 2008ha, while SN 2010ae, and other brighter SNe Iax, exhibit calcium lines at a later phase. At any rate, the fainter SNe 2019gsc and 2008ha are spectroscopically similar, if compared at different phases, to the equally faint SN 2010ae and to brighter objects such as SNe 2002cx and 2014ck, plotted in Fig. 9. More explicitly, the spectra of SNe 2008ha and 2019gsc  $\gtrsim 1$  month post maximum share the general shape (mostly because of the features content) as other SNe Iax at phases  $\gtrsim 5 - 6$  months post maximum.

However, as highlighted by [Foley et al. \(2016\)](#), there is also significant diversity in the late-time spectra of SN Iax class, especially in the strength, width and line shifts of forbidden emissions, such as [Ca II]  $\lambda\lambda 7291, 7324$ , [Fe II]  $\lambda 7155$ , and [Ni II]  $\lambda 7378$ . [Foley et al. \(2016\)](#) proposed a two-component model where the photosphere, P Cygni, and narrow forbidden lines are produced by the wind – which could be caused by the bound remnant of the progenitor WD and driven by the  $^{56}\text{Ni}$  left in such a remnant –, while the broad forbidden lines come from the SN ejecta. In this perspective, SN 2019gsc belongs to a low-velocity, narrow-[Ca II], [Ni II]-poor group (cf. Fig. 9), as well as SN 2008ha, but also

the bright prototype Iax SN 2002cx ([Foley et al. 2016](#), cf. their Section 3). The deflagration of a  $M_{Ch}$  hybrid C/O/Ne WD, leaving behind a bound remnant ([Kromer et al. 2015](#)) might produce faint transients (i.e., having peak absolute  $B$  magnitudes in the range  $-13.2$  to  $-14.4$  mag) with observational characteristics similar to both SNe 2008ha and 2019gsc, though there are shortcomings, for example the spectro-photometric evolution of the model is too fast. A possible alternative is the merger of a O/Ne and C/O WD (double-degenerate channel) that yields a failed detonation and produces a very faint, rapidly fading transient (actually fainter than SNe 2008ha, 2010ae and 2019gsc) with a small  $^{56}\text{Ni}$  and ejecta mass (see [Kashyap et al. 2018](#), for details). In support of the single-degenerate SN Iax progenitor scenario come the recent works of [Vennes et al. \(2017\)](#) and [Raddi et al. \(2019\)](#), with the discovery of a handful of high proper motion, low-mass Galactic WDs traveling at a velocity greater than the Milky Way escape velocity and whose peculiar atmospheres are dominated by IMEs. The authors argue that these inflated and IME contaminated WDs are the partially burnt remnants of SNe Iax, ejected from a binary SN progenitor with a high kick velocity.

Overall, the balance of evidence seems to suggest that SNe Iax are associated with the partial disruption of their progenitor stars, even if few works seem to suggest that the brightest members of the class may be linked to the full disruption of a Chandrasekhar mass WD (e.g., [Sahu et al. 2008](#); [Stritzinger et al. 2015](#)). Anyway, further study of both exceptionally faint and bright SNe Iax is critical to constrain the progenitors and the explosion mechanisms of this class of transients.

## ACKNOWLEDGEMENTS

Special thanks to the GTC Director and Support Staff for executing observations under director discretionary program DDT-GTC2019-129 (P.I. N. Elias-Rosa). M.S. is supported by a generous grant (13261) from the VILLUM FONDEN and a project grant from the Independent Research Fund Denmark (IRFD; 8021-00170B). K.M. acknowledges support from H2020 ERC grant no. 758638. Based on observations made with the Gran Telescopio Canarias (GTC), installed in the Spanish Observatorio del Roque de los Muchachos of the Instituto de Astrofísica de Canarias, in the island of La Palma. This work is partly based on NUTS2 observations made with the NOT (program 59-506), operated by the NOT Scientific Association at the Observatorio del Roque de los Muchachos, La Palma, Spain, of IAC. ALFOSC is provided by IAA under a joint agreement with the University of Copenhagen and NOTSA. NUTS2 is funded in part by the Instrument Center for Danish Astrophysics (IDA). The classification spectrum of SN 2019gsc was obtained with the Nordic Optical Telescope (program 59-509), operated by the Nordic Optical Telescope Scientific Association at the Observatorio del Roque de los Muchachos, La Palma, Spain, of the Instituto de Astrofísica de Canarias, and was kindly made available by S. Srivastav, D. Malesani, G. Leloudas. This work made use of ZTF data. We thank ZTF for access to this valuable public data stream and *Lasair* (<https://lasair.roe.ac.uk/>) which provides a broker system for users to access, visualise and extract science

data. Finally, we thank the anonymous Reviewer for the careful revision of the manuscript and the detailed and helpful feedback, which lead to a significant improvement of the manuscript.

## REFERENCES

- Aguado D. S., et al., 2019, *ApJS*, 240, 23  
 Arnett W. D., 1982, *ApJ*, 253, 785  
 Asplund M., Grevesse N., Sauval A. J., Scott P., 2009, *ARA&A*, 47, 481  
 Branch D., Baron E., Thomas R. C., Kasen D., Li W., Filippenko A. V., 2004, *PASP*, 116, 903  
 Brown P. J., et al., 2009, *AJ*, 137, 4517  
 Cardelli J. A., Clayton G. C., Mathis J. S., 1989, *ApJ*, 345, 245  
 Chomiuk L., et al., 2016, *ApJ*, 821, 119  
 Chornock R., Filippenko A. V., Branch D., Foley R. J., Jha S., Li W., 2006, *PASP*, 118, 722  
 Dessart L., Hillier D. J., 2015, *MNRAS*, 447, 1370  
 Dopita M. A., Kewley L. J., Sutherland R. S., Nicholls D. C., 2016, *Ap&SS*, 361, 61  
 Filippenko A. V., Foley R. J., Silverman J. M., Chornock R., Li W., Blondin S., Matheson T., 2007, *CBET*, 926, 1  
 Fink M., et al., 2014, *MNRAS*, 438, 1762  
 Firth R. E., et al., 2015, *MNRAS*, 446, 3895  
 Folatelli G., et al., 2012, *ApJ*, 745, 74  
 Foley R. J., et al., 2009, *AJ*, 138, 376  
 Foley R. J., et al., 2013, *ApJ*, 767, 57  
 Foley R. J., Jha S. W., Pan Y.-C., Zheng W. K., Bildsten L., Filippenko A. V., Kasen D., 2016, *MNRAS*, 461, 433  
 Harutyunyan A. H., et al., 2008, *A&A*, 488, 383  
 Hoeflich P., Khokhlov A., Mueller E., 1992, *A&A*, 259, 549  
 Huchtmeier W. K., Petrosian A., Gopal-Krishna, McLean B., Kunth D., 2008, *A&A*, 492, 367  
 Jacobson-Galán W. V., et al., 2019, *MNRAS*, 487, 2538  
 Jha S., et al., 2006, *AJ*, 132, 189  
 Jha S. W., 2017, *hsn..book*, 375, *hsn..book*  
 Jordan G. C., Perets H. B., Fisher R. T., van Rossum D. R., 2012, *ApJL*, 761, L23  
 Kashyap R., Haque T., Lorén-Aguilar P., García-Berro E., Fisher R., 2018, *ApJ*, 869, 140  
 Kerzendorf W. E., Sim S. A., 2014, *MNRAS*, 440, 38  
 Kromer M., et al., 2013, *MNRAS*, 429, 2287  
 Kromer M., et al., 2015, *MNRAS*, 450, 3045  
 Kulkarni S. R., 2018, *ATel*, 11266, 1  
 Leloudas G., et al., 2019, *TNSAN*, 25, 1  
 Li W., et al., 2003, *PASP*, 115, 453  
 Liu W.-M., Chen W.-C., Wang B., Han Z. W., 2010, *A&A*, 523, A3  
 Lyman J. D., Taddia, F., Stritzinger, M., et al., 2018, *MNRAS*, 473, 1359  
 Magee M. R., et al., 2016, *A&A*, 589, A89  
 Magee M. R., Sim S. A., Kotak R., Maguire K., Boyle A., 2019, *A&A*, 622, A102  
 Marino R. A., et al., 2013, *A&A*, 559, A114  
 McCully C., et al., 2014, *Natur*, 512, 54  
 Moriya T., et al., 2010, *ApJ*, 719, 1445  
 Moriya T. J., Eldridge J. J., 2016, *MNRAS*, 461, 2155  
 Mould J. R., et al., 2000, *ApJ*, 529, 786  
 Nomoto K., Kamiya Y., Nakasato N., 2013, *IAUS*, 253, *IAUS..281*  
 Nonaka A., Aspden A. J., Zingale M., Almgren A. S., Bell J. B., Woosley S. E., 2012, *ApJ*, 745, 73  
 Parrent J. T., et al., 2011, *ApJ*, 732, 30  
 Pettini M., Pagel B. E. J., 2004, *MNRAS*, 348, L59  
 Phillips M. M., 1993, *ApJL*, 413, L105  
 Phillips M. M., et al., 2007, *PASP*, 119, 360  
 Piro A. L., Nakar E., 2014, *ApJ*, 784, 85  
 Raddi R., et al., 2019, *MNRAS*, 489, 1489  
 Riess A. G., et al., 1999, *AJ*, 118, 2675  
 Riess A. G., et al., 2016, *ApJ*, 826, 56  
 Sahu D. K., et al., 2008, *ApJ*, 680, 580  
 Schlafly E. F., Finkbeiner D. P., 2011, *ApJ*, 737, 103  
 Smartt S. J., et al., 2019, *TNSAN*, 23, 1  
 Smith K. W., et al., 2019, *RNAAS*, 3, 26  
 Srivastav S., et al., 2020, *ApJL*, 892, L24  
 Stritzinger M., Leibundgut B., 2005, *A&A*, 431, 423  
 Stritzinger M. D., et al., 2014, *A&A*, 561, A146  
 Stritzinger M. D., et al., 2015, *A&A*, 573, A2  
 Taubenberger S., 2017, *hsn..book*, 317, *hsn..book*  
 Taubenberger S., et al., 2019, *MNRAS*, 488, 5473  
 Tomasella L., et al., 2016, *MNRAS*, 459, 1018  
 Tonry J. L., et al., 2018, *PASP*, 130, 064505  
 Valenti S., et al., 2009, *Natur*, 459, 674  
 Vennes S., Nemeth P., Kawka A., Thorstensen J. R., Khalack V., Ferrario L., Alper E. H., 2017, *Sci*, 357, 680

This paper has been typeset from a  $\text{\TeX}/\text{\LaTeX}$  file prepared by the author.